2020/05/29
Archive Hash: 7867c83-D
Archive Date: 2020/05/29

Measurement of pp $\to$ ZZ production cross sections and constraints on anomalous triple gauge couplings at $\sqrt{s} = 13$ TeV

The CMS Collaboration

Abstract

The production of Z-boson pairs in proton-proton collisions, pp $\to (\mathrm{Z}/\gamma^*)(\mathrm{Z}/\gamma^*) \to 2\ell 2\ell'$, where ℓ, ℓ' = e or μ, is studied at a center-of-mass energy of 13 TeV with the CMS detector at the LHC. The data sample corresponds to an integrated luminosity of 137 fb^{-1}, collected during 2016–2018. The ZZ production cross section, $\sigma_{tot}(pp \to ZZ) = 17.2 \pm 0.3\,(\text{stat}) \pm 0.5\,(\text{syst}) \pm 0.4\,(\text{theo}) \pm 0.3\,(\text{lumi})$ pb, measured for events with two opposite-sign, same-flavor lepton pairs produced in the mass region $60 < m_{\ell^+\ell^-} < 120$ GeV is consistent with standard model predictions. Differential cross sections are measured and agree with theoretical predictions. The invariant mass distribution of the four-lepton system is used to set limits on anomalous ZZZ and ZZγ couplings at the 95% confidence level.

1 Introduction

Measurements of diboson production at the CERN LHC allow precision tests of the standard model (SM). In the SM, ZZ production proceeds mainly through quark-antiquark t- and u-channel scattering diagrams. In calculations at higher orders in quantum chromodynamics (QCD), gluon-gluon fusion also contributes via box diagrams with quark loops. There are no tree-level contributions to ZZ production from triple gauge boson vertices in the SM. Anomalous triple gauge couplings (aTGC) ZZZ and ZZγ are introduced using an effective Lagrangian following Ref. [1]. In this parametrization, two ZZZ and two ZZγ couplings are allowed by electromagnetic gauge invariance and Lorentz invariance for on-shell Z bosons and are parametrized by two CP-violating (f_4^{V}) and two CP-conserving (f_5^{V}) parameters, where $\mathrm{V} = (\mathrm{Z}, \gamma)$. Nonzero aTGC values could be induced by new physics models such as supersymmetry [2].

Previous measurements of the production cross section for pairs of on-shell Z bosons were performed by the CMS Collaboration with data sets corresponding to integrated luminosities of 5.1 fb^{-1} at $\sqrt{s} = 7$ TeV [3] and 19.6 fb^{-1} at $\sqrt{s} = 8$ TeV [4, 5] in the $\mathrm{ZZ} \to 2\ell 2\ell''$ and $\mathrm{ZZ} \to 2\ell 2\nu$ decay channels, where $\ell = \mathrm{e}$ or μ and $\ell'' = \mathrm{e}, \mu$, or τ; and with an integrated luminosity of 2.6 fb^{-1} [6] and 35.9 fb^{-1} [7] at $\sqrt{s} = 13$ TeV in the $\mathrm{ZZ} \to 2\ell 2\ell'$ decay channel, where $\ell' = \mathrm{e}$ or μ. All of the results agree with SM predictions. The ATLAS collaboration reported similar results at $\sqrt{s} = 7$, 8, and 13 TeV [8–13], which also agree with SM predictions. These measurements are important to test predictions that were recently made available at next-to-next-to-leading order (NNLO) in QCD [14]. Comparing these predictions to data for a range of center-of-mass energies provides insight into the structure of the electroweak gauge sector of the SM.

This paper reports a study of the ZZ production in the four-lepton decay channel ($\mathrm{pp} \to 2\ell 2\ell'$, where $\ell\ell$ and $\ell'\ell'$ indicate opposite-sign pairs of electrons or muons) at $\sqrt{s} = 13$ TeV with a data set corresponding to an integrated luminosity of 137 fb^{-1} recorded in 2016–2018. Both Z bosons are produced on-shell, defined as the mass range 60–120 GeV. The invariant mass distribution of the four-lepton system is used to set limits on anomalous ZZZ and ZZγ couplings at the 95% confidence level (CL).

2 The CMS detector

A detailed description of the CMS detector, together with a definition of the coordinate system used and the relevant kinematic variables, can be found in Ref. [15].

The central feature of the CMS apparatus is a superconducting solenoid of 6 m internal diameter, providing a magnetic field of 3.8 T. Within the solenoid volume are a silicon pixel and strip tracker, a lead tungstate crystal electromagnetic calorimeter (ECAL), and a brass and scintillator hadron calorimeter, which provide coverage in pseudorapidity $|\eta| < 1.479$ in a cylindrical barrel and $1.479 < |\eta| < 3.0$ in two endcap regions. Forward calorimeters extend the coverage provided by the barrel and endcap detectors to $|\eta| < 5.0$. Muons are detected in gas-ionization detectors embedded in the steel flux-return yoke outside the solenoid in the range $|\eta| < 2.4$, with detection planes made using three technologies: drift tubes, cathode strip chambers, and resistive plate chambers.

Electron momenta are estimated by combining energy measurements in the ECAL with momentum measurements in the tracker. The momentum resolution for electrons with transverse momentum $p_{\mathrm{T}} \approx 45$ GeV from $\mathrm{Z} \to \mathrm{e}^+\mathrm{e}^-$ decays ranges from 1.7% for nonshowering electrons in the barrel region to 4.5% for showering electrons in the endcaps [16]. Match-

ing muons to tracks identified in the silicon tracker results in a p_T resolution for muons with $20 < p_T < 100\,\text{GeV}$ of 1.3–2.0% in the barrel and better than 6% in the endcaps. The p_T resolution in the barrel is better than 10% for muons with p_T up to 1 TeV [17, 18].

3 Signal and background simulation

Signal events are generated with POWHEG 2.0 [19–23] at next-to-leading order (NLO) in QCD for quark-antiquark processes and leading order (LO) for quark-gluon processes. This includes ZZ, $Z\gamma^*$, Z, $\gamma^*\gamma^*$, and SM Higgs production with a constraint of $m_{\ell\ell'} > 4\,\text{GeV}$ applied to all pairs of oppositely charged leptons at the generator level to avoid infrared divergences. No merging is applied. The $gg \to ZZ$ loop-induced process is simulated at LO with MCFM v7.0 [24]. The cross sections are scaled to correspond to cross section values calculated at NNLO in QCD for $q\bar{q} \to ZZ$ [14] (with a K factor of 1.1) and at NLO in QCD for $gg \to ZZ$ and $gg \to H$ [25] (K factor of 1.7). The Higgs boson decay is modeled with JHUGEN 3.1.8 [26–28] at LO. Higgs contribution to the total number of events in the phase space of this analysis is less than one percent.

Samples of events for background processes containing three or four prompt leptons in the final state, like $t\bar{t}Z$, WWZ and WZ production, are produced with MADGRAPH5_aMC@NLO v2.4.2 [29] at NLO with zero or one outgoing partons at the Born level, merged using the FxFx scheme [30].

Samples with aTGC contributions included are generated at LO with SHERPA v2.1.1 [31]. The distributions from the SHERPA samples are normalized such that the total yield of the SM sample is the same as that of the POWHEG sample.

The PYTHIA v8.175 [22, 32] package is used for parton showering, hadronization, and the underlying event simulation, with parameters sets by the CP5 [33] and CUETP8M1 [34] tunes with NNPDF 31_nnlo_as_0118 [35] and NNPDF31_lo_as_0130 respectively.

The detector response is simulated using a detailed description of the CMS detector implemented with the GEANT4 package [36]. The event reconstruction is performed with the same algorithms used for data. The simulated samples include additional interactions per bunch crossing, referred to as pileup. The simulated events are weighted so that the pileup distribution matches the data.

4 Event reconstruction

All stable particles – electrons, muons, photons, and charged and neutral hadrons – in each collision event are identified and reconstructed with the CMS particle-flow (PF) algorithm [37] from a combination of the signals from all subdetectors. Reconstructed electrons [16] and muons [17] are considered as lepton candidates if they have $p_T^e > 7\,\text{GeV}$ and $|\eta^e| < 2.5$ or $p_T^\mu > 5\,\text{GeV}$ and $|\eta^\mu| < 2.4$.

Lepton candidates are also required to originate from the event vertex, defined as the reconstructed proton-proton interaction vertex with the largest value of summed physics object p_T^2. The physics objects used in the event vertex definition are the objects returned by a jet finding algorithm [38, 39] applied to all charged tracks associated with the vertex, plus the corresponding associated missing transverse momentum [40]. The distance of closest approach between each lepton track and the event vertex is required to be less than 0.5 cm in the plane transverse to the beam axis, and less than 1 cm in the direction along the beam axis. Furthermore, the

significance of the three-dimensional impact parameter relative to the event vertex, SIP_{3D}, is required to satisfy $\mathrm{SIP}_{3D} \equiv |\mathrm{IP}/\sigma_{\mathrm{IP}}| < 4$ for each lepton, where IP is the distance of closest approach of each lepton track to the event vertex and σ_{IP} is its associated uncertainty.

Lepton candidates are required to be isolated from other particles in the event. The relative isolation is defined as

$$R_{\mathrm{iso}} = \left[\sum_{\substack{\text{charged}\\ \text{hadrons}}} p_{\mathrm{T}} + \max\left(0, \sum_{\substack{\text{neutral}\\ \text{hadrons}}} p_{\mathrm{T}} + \sum_{\text{photons}} p_{\mathrm{T}} - p_{\mathrm{T}}^{\mathrm{PU}}\right)\right] \Big/ p_{\mathrm{T}}^{\ell}, \tag{1}$$

where the sums run over the charged and neutral hadrons and photons identified by the PF algorithm, in a cone defined by $\Delta R \equiv \sqrt{(\Delta\eta)^2 + (\Delta\phi)^2} < 0.3$ around the lepton momentum direction, where ϕ is the azimuthal angle in radians. To minimize the contribution of charged particles from pileup to the isolation calculation, charged hadrons are included only if they originate from the event vertex. The contribution of neutral particles from pileup is $p_{\mathrm{T}}^{\mathrm{PU}}$. For electrons, $p_{\mathrm{T}}^{\mathrm{PU}}$ is evaluated with the "jet area" method described in Ref. [41]; for muons, it is half the sum of the p_{T} of all charged particles in the cone originating from pileup vertices. The factor of one-half accounts for the expected ratio of charged to neutral particle energy in hadronic interactions. A lepton is considered isolated if $R_{\mathrm{iso}} < 0.35$.

The lepton reconstruction, identification, and isolation efficiencies are measured with a "tag-and-probe" technique [42] applied to a sample of $\mathrm{Z} \to \ell^+\ell^-$ data events. The measurements are performed in several bins of p_{T}^{ℓ} and $|\eta^{\ell}|$. The electron reconstruction and selection efficiency in the ECAL barrel (endcaps) varies from about 85% (77%) at $p_{\mathrm{T}}^{\mathrm{e}} \approx 10\,\mathrm{GeV}$ to about 95% (89%) for $p_{\mathrm{T}}^{\mathrm{e}} \geq 20\,\mathrm{GeV}$, while in the barrel-endcap transition region this efficiency is about 85% averaged over electrons with $p_{\mathrm{T}}^{\mathrm{e}} > 7\,\mathrm{GeV}$. The muons are reconstructed and identified with efficiencies above ~98% within $|\eta^{\mu}| < 2.4$.

5 Event selection

The primary triggers for this analysis require the presence of a pair of loosely isolated leptons of the same or different flavors [43]. The highest p_{T} lepton must have $p_{\mathrm{T}}^{\ell} > 17\,\mathrm{GeV}$, and the subleading lepton must have $p_{\mathrm{T}}^{\mathrm{e}} > 12\,\mathrm{GeV}$ if it is an electron or $p_{\mathrm{T}}^{\mu} > 8\,\mathrm{GeV}$ if it is a muon. The tracks of the triggering leptons are required to originate within 2 mm of each other in the plane transverse to the beam axis. Triggers requiring a triplet of lower-p_{T} leptons with no isolation criterion, or a single high-p_{T} electron or muon, are also used. An event is used if it passes any trigger regardless of the decay channel. The total trigger efficiency for events within the acceptance of this analysis is greater than 98%.

The four-lepton candidate selection is based on the one used in the recent Higgs analysis [44]. A signal event must contain at least two Z/γ^* candidates, each formed from an oppositely charged pair of isolated electron or muon candidates. Among the four leptons, the highest p_{T} lepton must have $p_{\mathrm{T}} > 20\,\mathrm{GeV}$, and the second-highest p_{T} lepton must have $p_{\mathrm{T}}^{\mathrm{e}} > 12\,\mathrm{GeV}$ if it is an electron or $p_{\mathrm{T}}^{\mu} > 10\,\mathrm{GeV}$ if it is a muon. All leptons are required to be separated from each other by $\Delta R(\ell_1, \ell_2) > 0.02$, and electrons are required to be separated from muons by $\Delta R(\mathrm{e}, \mu) > 0.05$.

Within each event, all permutations of leptons giving a valid pair of Z/γ^* candidates are considered separately. Within each four-lepton candidate, the dilepton candidate with an invariant mass closest to 91.2 GeV, taken as the nominal Z boson mass [45], is denoted Z_1 and is required to have a mass greater than 40 GeV. The other dilepton candidate is denoted Z_2 and is required

to have a mass greater than 4 GeV. Both m_{Z_1} and m_{Z_2} are required to be less than 120 GeV. All pairs of oppositely charged leptons in the 4ℓ candidate are required to have $m_{\ell\ell'} > 4$ GeV regardless of their flavor.

If multiple four-lepton candidates within an event satisfy the above criteria, the one with m_{Z_1} closest to the nominal Z boson mass is chosen. In the rare case of further ambiguity, which occurs in less than 0.5% of events when five or more passing lepton candidates are found, the Z_2 candidate that maximizes the scalar p_T sum of the four leptons is chosen.

The $pp \to ZZ$ cross section is measured using events where both m_{Z_1} and m_{Z_2} are greater than 60 GeV. Decays of the Z bosons to τ leptons with subsequent decays to electrons and muons are heavily suppressed by the requirements on lepton p_T, and the contribution of such events is less than 0.5% of the total ZZ yield. If these events pass the selection requirements of the analysis, they are considered signal, while they are not considered at generator level in the cross section measurement procedure. Thus, the correction for possible τ decays is included in the efficiency calculation. The same is done for the expected small contribution of Higgs events.

6 Background estimation

The requirement of four well reconstructed and isolated lepton candidates heavily suppresses any background, therefore this analysis has very low background contributions. The major background contributions arise from Z boson and WZ diboson production in association with jets and from $t\bar{t}$ production. In all these cases, particles from jet fragmentation satisfy both lepton identification and isolation criteria, and are thus misidentified as signal leptons.

The probability for such objects to be selected is measured from a sample of $Z + \ell_{\text{candidate}}$ events, where Z denotes a pair of oppositely charged, same-flavor leptons that pass all analysis requirements and satisfy $|m_{\ell^+\ell^-} - m_Z| < 10$ GeV, where m_Z is the nominal Z boson mass. Each event in this sample must have exactly one additional object $\ell_{\text{candidate}}$ that passes relaxed identification requirements with no isolation requirements applied. The misidentification probability for each lepton flavor, measured in bins of lepton candidate p_T and η, is defined as the ratio of the number of candidates that pass the final isolation and identification requirements to the total number of candidates in the sample. The number of $Z + \ell_{\text{candidate}}$ events is corrected for the contamination from WZ production and ZZ production in which one lepton is not reconstructed. These events have a third genuine, isolated lepton that must be excluded from the misidentification probability calculation. The WZ contamination is suppressed by requiring the missing transverse momentum p_T^{miss} to be below 25 GeV. The p_T^{miss} is defined as the magnitude of the missing transverse momentum vector $\vec{p}_T^{\text{miss}}$, the projection onto the plane transverse to the beams of the negative vector sum of the momenta of all reconstructed PF candidates in the event, corrected for the jet energy scale. Additionally, the transverse mass calculated with $\vec{p}_T^{\text{miss}}$ and the $\vec{p}_T$ of $\ell_{\text{candidate}}$, $m_T \equiv \sqrt{(p_T^{\ell} + p_T^{\text{miss}})^2 - (\vec{p}_T^{\,\ell} + \vec{p}_T^{\text{miss}})^2}$, is required to be less than 30 GeV. The residual contribution of WZ and ZZ events, which can be up to a few percent of the events with $\ell_{\text{candidate}}$ passing all selection criteria, is estimated from simulation and subtracted.

To account for all sources of background events, two control samples are used to estimate the number of background events in the signal regions. Both are defined as samples that contain events with a dilepton candidate satisfying all requirements (Z_1) and two additional lepton candidates $\ell^+\ell^-$. In one control sample, enriched in WZ events, one ℓ candidate is required to satisfy the full identification and isolation criteria and the other must fail the full criteria and instead satisfy only the relaxed ones; in the other, enriched in Z+jets events, both ℓ can-

didates must satisfy the relaxed criteria, but fail the full criteria. The additional leptons must have opposite charge and the same flavor ($e^{\pm}e^{\mp}$, $\mu^{\pm}\mu^{\mp}$). From this set of events, the expected number of background events in the signal region, denoted "Z + X" in the figures, is obtained by scaling the number of observed $Z_1 + \ell^+\ell^-$ events by the misidentification probability for each lepton failing the selection. The procedure is described in more detail in Ref. [44].

In addition to these nonprompt backgrounds, $t\bar{t}Z$ and WWZ processes contribute a smaller number of events with four prompt leptons, which is estimated from simulated samples to be around 1% of the expected $ZZ \to 2\ell 2\ell'$ yield. The total background contributions to the $ZZ \to 2\ell 2\ell'$ signal regions are summarized in Section 8.

7 Systematic uncertainties

The major sources of systematic uncertainty and their effect on the measured cross sections are summarized in Table 1. In both data and simulated event samples, trigger efficiencies are evaluated with a tag-and-probe technique. The ratio of data to simulation estimated trigger efficiencies is applied to simulated events, and the size of the resulting change in expected yield is taken as the uncertainty in the determination of the trigger efficiency. This uncertainty is around 2% of the final estimated yield.

Table 1: The contributions of each source of systematic uncertainty in the cross section measurements. The integrated luminosity uncertainty, and the PDF and scale uncertainties, are considered separately. All other uncertainties are added in quadrature into a single systematic uncertainty. Uncertainties that vary by decay channel are listed as a range.

Uncertainty	Range of values
Lepton efficiency	2–8%
Trigger efficiency	1–2%
Background	0.6–1.3%
Pileup	1%
PDF	1%
NNLO/NLO corrections	1%
μ_R, μ_F	1%
Integrated luminosity	2.5% (2016), 2.3% (2017), 2.5% (2018)

The lepton identification, isolation, and track reconstruction efficiencies in simulation are corrected with scaling factors derived with a tag-and-probe method and applied as a function of lepton p_T and η. To estimate the uncertainties associated with the tag-and-probe technique, the total yield is recomputed with the scaling factors varied up and down by the tag-and-probe fit uncertainties. The uncertainties associated with lepton efficiency in the $ZZ \to 2\ell 2\ell'$ signal regions are found to be 5% in the 4e, 3% in the 2e2μ, and 2% in the 4μ final states.

Uncertainties due to the effect of factorization (μ_F) and renormalization (μ_R) scale choices on the $ZZ \to 2\ell 2\ell'$ acceptance are evaluated with POWHEG and MCFM by varying the QCD scales up and down by a factor of two with respect to the default values $\mu_F = \mu_R = m_{ZZ}$. All combinations are considered except those in which μ_F and μ_R differ by a factor of four. Parametric uncertainties (PDF+α_s) are evaluated according to the PDF4LHC prescription [46] in the acceptance calculation, and with NNPDF3.0 [47] in the cross section calculations. An additional theoretical uncertainty arises from scaling the POWHEG $q\bar{q} \to ZZ$ simulated sample from its NLO cross section to the NNLO prediction, and the MCFM $gg \to ZZ$ samples from their LO cross sections to the NLO predictions. The change in the acceptance corresponding to this scaling procedure is about 1%.

The largest uncertainty in the estimated background yield arises from differences in sample composition between the $Z + \ell_{\text{candidate}}$ control sample used to calculate the lepton misidentification probability and the $Z + \ell^+\ell^-$ control sample. A further uncertainty arises from the limited number of events in the $Z + \ell_{\text{candidate}}$ sample. A systematic uncertainty of 40% is applied to the lepton misidentification probability to cover both effects. Its impact varies by channel, but is of the order of 1% of the total expected yield.

The uncertainty in the integrated luminosity of the data samples is 2.5% (2016) [48], 2.3% (2017) [49], and 2.5% (2018) [50].

8 Cross section measurement

The distribution of the invariant mass of the ZZ system, individual mass of reconstructed Z boson candidates in ZZ events, and their corresponding p_{T} distributions are shown in Fig. 1. The p_{T} and η distributions for individual leptons are shown in Fig. 2. These distributions are shown for data and simulated events to allow comparison to SM expectations. The expectations include contributions from the nonresonant ZZ production normalized to the NNLO cross sections, and from the SM Higgs boson with mass 125 GeV production. The reducible background estimated from data is also shown. The measured and expected event yields for all decay channels are summarized in Table 2.

The measured yields are used to evaluate the ZZ production cross section in the fiducial phase space. The signal acceptance is evaluated from simulation and corrected for each individual lepton flavor in bins of p_{T} and η using factors obtained with the tag-and-probe technique. The branching fraction $BR_{\text{Z}\to\ell\ell}$ is $3.3658 \pm 0.0023\%$ is used for each lepton flavor [45].

To include all final states in the cross section calculation a simultaneous fit to the number of observed events in all decay channels is performed. The likelihood is written as a combination of individual channel likelihoods for the signal and background hypotheses with the statistical and systematic uncertainties treated as scaling nuisance parameters. The combination of various data taking periods is performed treating the theoretical uncertainties as fully correlated among various periods, while the experimental uncertainties are either correlated or uncorrelated depending on their origin.

The fiducial phase spaces for the $\text{ZZ} \to 2\ell 2\ell'$ cross section measurements is defined as: $p_{\text{T}}^{\ell_1} > 20\,\text{GeV}$, $p_{\text{T}}^{\ell_2} > 10\,\text{GeV}$, $p_{\text{T}}^{\ell_{3,4}} > 5\,\text{GeV}$, $|\eta^{\ell}| < 2.5$, $m_{\ell\ell} > 4\,\text{GeV}$ (any opposite-sign same-flavor pair), $60 < m_{\text{Z}_1}, m_{\text{Z}_2} < 120\,\text{GeV}$. The generator-level leptons used for the fiducial cross section calculation are "dressed" by adding the momenta of generator-level photons within $\Delta R\,(\ell, \gamma) < 0.1$ from the lepton momenta directions.

The measured ZZ fiducial cross section presented in Table 3 can be compared to $34.4^{+0.7}_{-0.6} \pm 0.5\,\text{fb}$ calculated with POWHEG and MCFM using the same settings as the simulated samples without K factors applied. The first uncertainty corresponds to the QCD scale variations and second to the PDF, as described above. The POWHEG calculations used dynamic QCD scales $\mu_{\text{F}} = \mu_{\text{R}} = m_{2\ell 2\ell'}$, while the contribution from MCFM is computed with dynamic QCD scales $\mu_{\text{F}} = \mu_{\text{R}} = 0.5 m_{2\ell 2\ell'}$.

The total ZZ production cross section for both dileptons produced in the mass range 60–120 GeV and $m_{\ell^+\ell^-} > 4\,\text{GeV}$ is presented in Table 4. The measured total cross section can be compared to the theoretical value of $14.5^{+0.5}_{-0.4} \pm 0.2\,\text{pb}$ calculated from a combination of POWHEG and MCFM with the same settings as used for $\sigma_{\text{fid}}(\text{pp} \to \text{ZZ} \to 2\ell 2\ell')$. It can also be compared to $16.2^{+0.6}_{-0.4}\,\text{pb}$, calculated at NNLO in QCD via MATRIX v1.0.0_beta4 [14, 51, 52], or

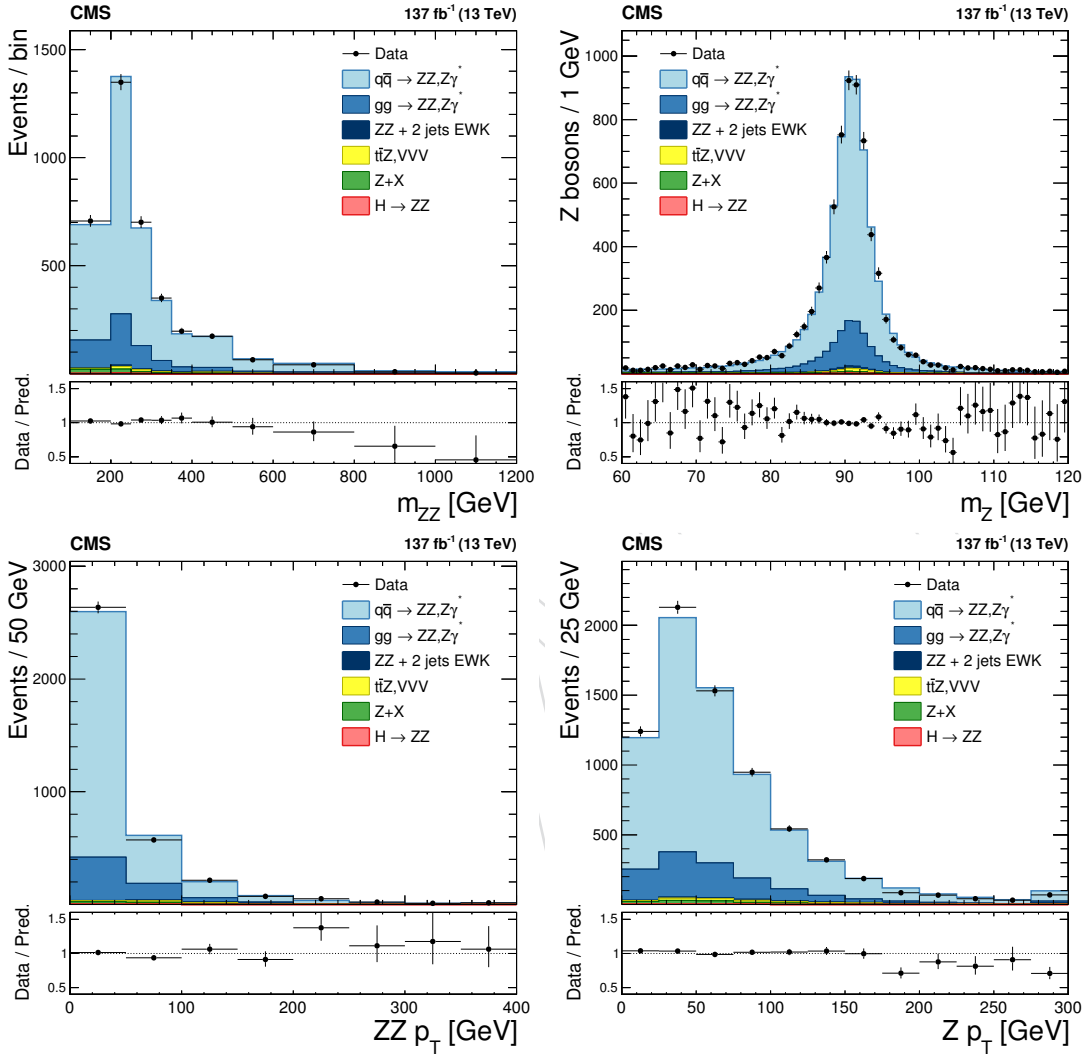

Figure 1: Distributions of (top-left) m_{ZZ} for ZZ events with $60 < m_{Z_1,Z_2} < 120\,\text{GeV}$; (top-right) mass of selected Z boson candidates; (bottom-left) transverse momentum of the ZZ system; (bottom-right) transverse momentum of individual Z boson candidates. The results correspond to an integrated luminosity of $137\,\text{fb}^{-1}$. Points represent the data, shaded histograms the expected SM predictions and reducible background estimated from data.

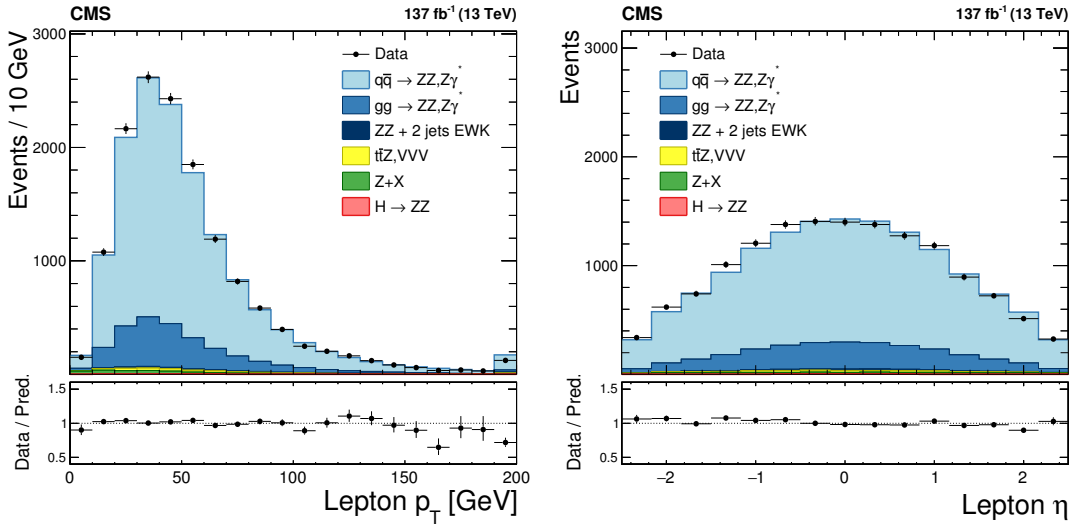

Figure 2: Distributions of (top-left) transverse momentum and (top-right) pseudorapidity for individual leptons. The results correspond to an integrated luminosity of 137 fb^{-1}. Points represent the data, shaded histograms the expected SM predictions and reducible background estimated from data.

Table 2: Observed and expected prefit yields of ZZ events, and estimated yields of background events, shown for each final state and combined. The statistical and systematic uncertainties are shown.

Process	eeee	ee$\mu\mu$	$\mu\mu\mu\mu$	$2\ell 2\ell'$
	2016			
Background	$8.3 \pm 0.6 \pm 1.8$	$15.6 \pm 0.8 \pm 1.9$	$8.1 \pm 0.5 \pm 0.9$	$32.1 \pm 1.1 \pm 4.1$
Signal	$167.0 \pm 1.0 \pm 10.0$	$432.0 \pm 1.6 \pm 17.3$	$272.0 \pm 1.3 \pm 8.2$	$870.9 \pm 2.3 \pm 31.1$
Total expected	$175.4 \pm 1.2 \pm 10.4$	$447.5 \pm 1.8 \pm 17.7$	$280.0 \pm 1.4 \pm 8.4$	$903.0 \pm 2.6 \pm 32.0$
Data	176	478	296	950
	2017			
Background	$8.2 \pm 0.4 \pm 1.5$	$16.8 \pm 0.8 \pm 1.8$	$10.9 \pm 0.7 \pm 1.6$	$35.8 \pm 1.2 \pm 4.5$
Signal	$199.7 \pm 0.3 \pm 12.0$	$509.7 \pm 0.6 \pm 20.4$	$320.7 \pm 0.5 \pm 9.6$	$1030.0 \pm 0.8 \pm 36.9$
Total expected	$207.9 \pm 0.6 \pm 12.4$	$526.5 \pm 1.0 \pm 20.9$	$331.5 \pm 0.8 \pm 9.9$	$1065.9 \pm 1.4 \pm 38.0$
Data	193	540	328	1061
	2018			
Background	$12.9 \pm 0.6 \pm 2.5$	$30.7 \pm 1.1 \pm 4.2$	$20.2 \pm 1.1 \pm 4.0$	$63.8 \pm 1.7 \pm 9.7$
Signal	$303.2 \pm 0.4 \pm 18.2$	$754.2 \pm 0.8 \pm 30.1$	$463.8 \pm 0.6 \pm 13.9$	$1521.3 \pm 1.0 \pm 54.7$
Total expected	$316.2 \pm 0.8 \pm 18.7$	$784.9 \pm 1.4 \pm 31.1$	$484.0 \pm 1.3 \pm 14.8$	$1585.0 \pm 2.0 \pm 56.6$
Data	309	797	480	1586

Table 3: Measured fiducial cross section for each data sample, and combined. The first uncertainty is experimental, second systematic and third on integrated luminosity.

Year	Fiducial cross section, fb
2016	$41.6 \pm 1.4\,(\text{stat}) \pm 1.3\,(\text{syst})^{+1.1}_{-1.0}\,(\text{lumi})$
2017	$39.2 \pm 1.2\,(\text{stat})^{+1.3}_{-1.2}\,(\text{syst})^{+1.0}_{-0.9}\,(\text{lumi})$
2018	$39.3 \pm 1.0\,(\text{stat})^{+1.3}_{-1.1}\,(\text{syst}) \pm 1.0\,(\text{lumi})$
Combined	$40.1 \pm 0.7\,(\text{stat}) \pm 1.1\,(\text{syst}) \pm 0.7\,(\text{lumi})$

Table 4: Measured total $\sigma(pp \to ZZ)$ cross section for each data sample, and combined. The first uncertainty is statistical, second experimental systematic, third theoretical and the last one on integrated luminosity.

Year	Total cross section, pb
2016	$17.9 \pm 0.6\,(\text{stat})^{+0.6}_{-0.5}\,(\text{syst}) \pm 0.4\,(\text{theo})^{+0.5}_{-0.4}\,(\text{lumi})$
2017	$16.8 \pm 0.5\,(\text{stat})^{+0.6}_{-0.5}\,(\text{syst}) \pm 0.4\,(\text{theo}) \pm 0.4\,(\text{lumi})$
2018	$16.9 \pm 0.4\,(\text{stat}) \pm 0.5\,(\text{syst}) \pm 0.4\,(\text{theo}) \pm 0.4\,(\text{lumi})$
Combined	$17.2 \pm 0.3\,(\text{stat}) \pm 0.5\,(\text{syst}) \pm 0.4\,(\text{theo}) \pm 0.3\,(\text{lumi})$

$15.0^{+0.7}_{-0.6} \pm 0.2$ pb, calculated with MCFM at NLO in QCD with additional contributions from LO $gg \to ZZ$ diagrams. Both values are calculated with the NNPDF3.0 PDF sets, at NNLO and NLO, respectively, and fixed QCD scales set to $\mu_F = \mu_R = m_Z$.

The total ZZ cross section is shown in Fig. 3 as a function of the proton-proton center-of-mass energy. Results from CMS [3, 4] and ATLAS [8, 9, 13] are compared to predictions from MATRIX and MCFM with the NNPDF3.0 PDF sets and fixed QCD scales $\mu_F = \mu_R = m_Z$. The MATRIX prediction uses PDFs calculated at NNLO, while the MCFM prediction uses NLO PDFs. The uncertainties are statistical (inner bars) and statistical and systematic combined, as obtained from the fit (outer bars). The band around the MATRIX predictions reflects scale uncertainties, while the band around the MCFM predictions reflects both scale and PDF uncertainties.

9 Differential cross sections

The differential distributions normalized to the fiducial cross sections are presented in Figs. 4–6 for the combination of the 4e, 4μ, and 2e2μ decay channels using the whole data sample. The fiducial cross section definition includes p_T^ℓ and $|\eta^\ell|$ selections on each lepton, and the 60–120 GeV mass requirement, as described in Section 4. Figure 4 shows the differential cross sections in bins of p_T for: (left) all leptons in the event, (right) both Zs in the event, and in Fig. 5 (left) for the p_T of the ZZ system. Figure 5 (right) shows the normalized $d\sigma/dm_{ZZ}$ distribution. The data are corrected for background contributions and unfolded for detector effects using a matrix inversion method without regularization as described in Ref. [53], and compared with the theoretical predictions from POWHEG +MCFM, MADGRAPH5_AMC@NLO+MCFM and MATRIX. The bottom part of each plot shows the ratio of the measured to the predicted values. The bin sizes were chosen according to the resolution of the relevant variables, trying also to keep the statistical uncertainties at a similar level for all the bins. Figure 6 shows the angular correlations between Z bosons. The POWHEG +MCFM and MADGRAPH5_AMC@NLO+MCFM predictions demonstrate good agreement with data. The MATRIX predictions show some deviation from the measurements as a function of p_T^{ZZ} and azimuthal separation between the two Z bosons.

10 Limits on anomalous triple gauge couplings

The presence of aTGCs would be manifested as an increased yield of events at high four-lepton masses. Figure 7 presents the distribution of the four-lepton reconstructed mass for the combined 4e, 4μ, and 2e2μ channels, for the SM and a working point with nonzero aTGC. Limits on aTGCs are derived from fits to this distribution. While the shaded histograms represent the SM predictions as described in the previous sections, the dashed curve shows the SHERPA prediction. The SHERPA SM part is normalized to the POWHEG and agrees well with it in shape

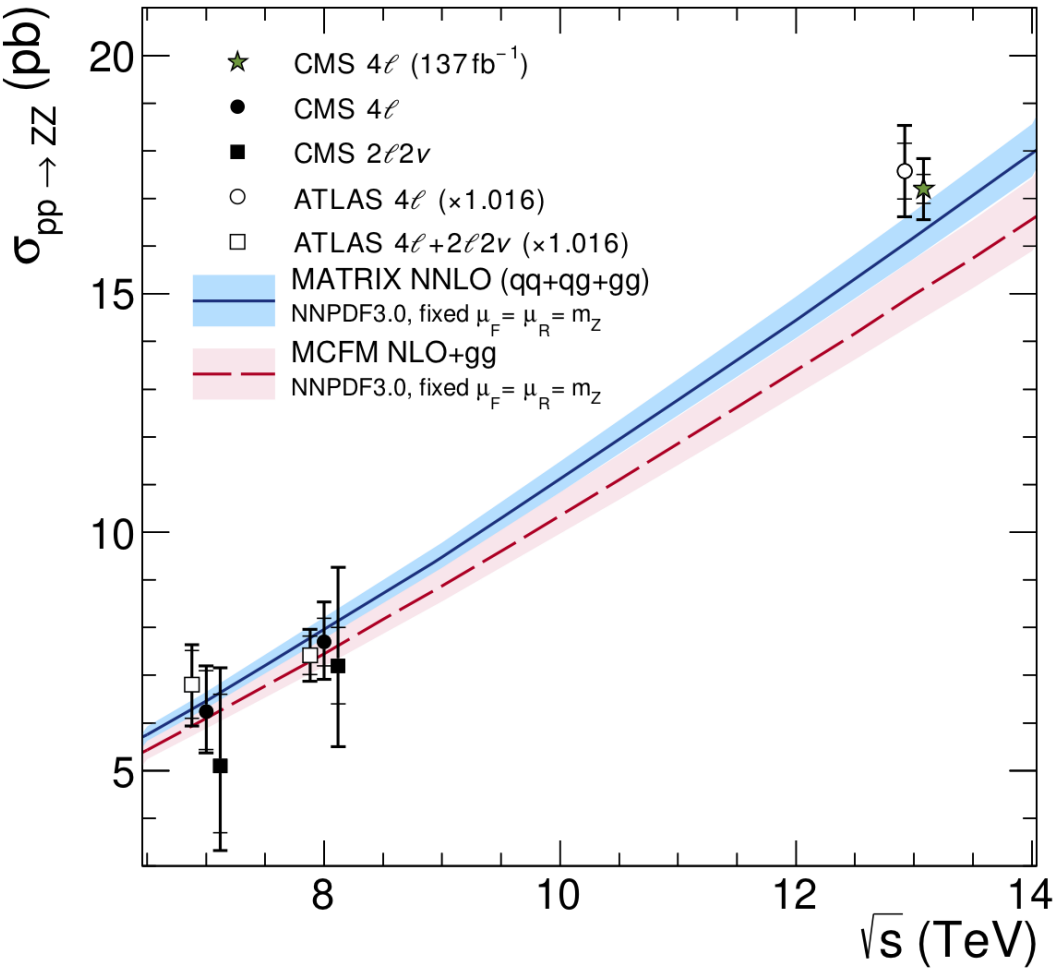

Figure 3: The total ZZ cross section as a function of the proton-proton center-of-mass energy. Results from the CMS [3, 4] and ATLAS [8, 9, 13] experiments are compared to predictions from MATRIX at NNLO in QCD, and MCFM at NLO in QCD. The MCFM prediction also includes gluon-gluon initiated production at LO in QCD. Both predictions use NNPDF3.0 PDF sets and fixed QCD scales $\mu_F = \mu_R = m_Z$. Details of the calculations and uncertainties are given in the text. The ATLAS measurements were performed with a Z boson mass window of 66–116 GeV, instead of 60–120 GeV used by CMS, and are corrected for the resulting 1.6% difference in acceptance. Measurements at the same center-of-mass energy are shifted slightly along the horizontal axis for clarity.

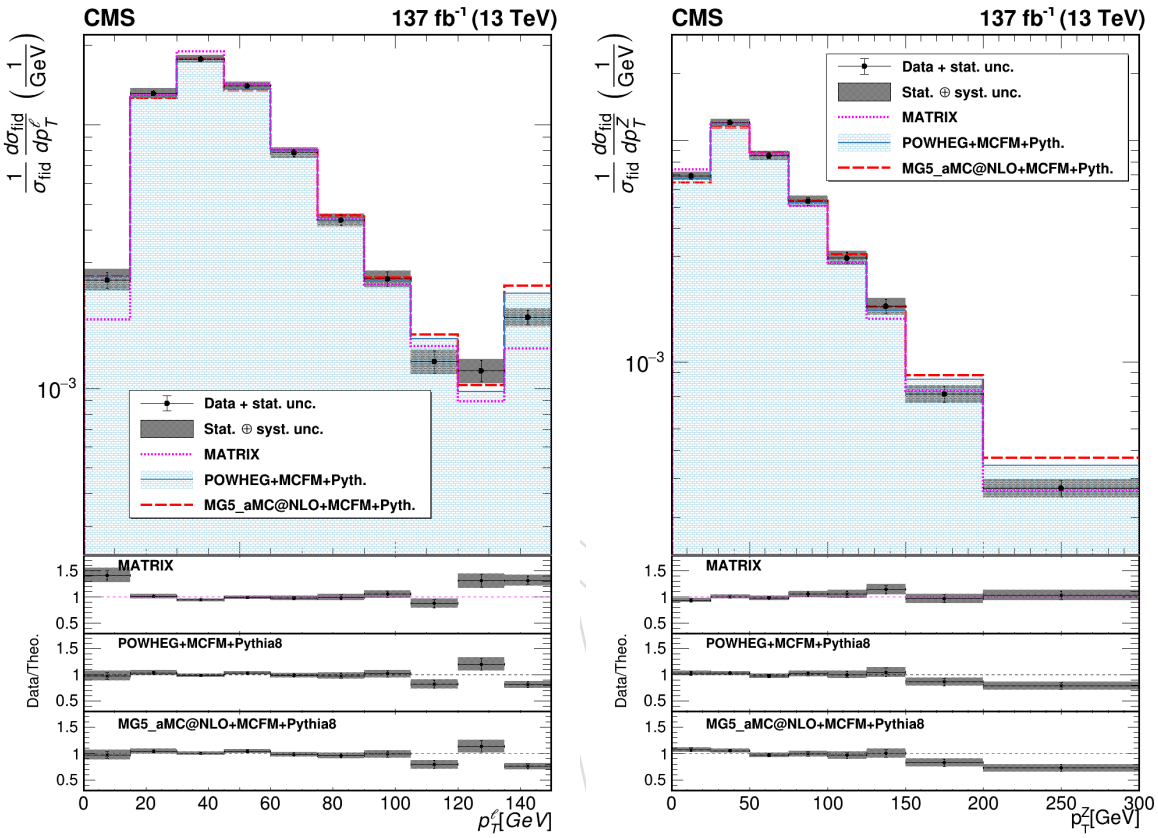

Figure 4: Differential cross sections normalized to the fiducial cross section for the combined 4e, 4μ, and 2e2μ decay channels as a function of p_{T} for (left) all leptons, (right) all Z bosons in the event. Points represent the unfolded data, the shaded histogram represent the POWHEG +MCFM ZZ predictions, and the dashed curves correspond to the results of the MATRIX and MADGRAPH5_AMC@NLO+MCFM calculations. The three lower panels represent the ratio of the measured cross section to the expected distributions from MATRIX, POWHEG +MCFM and MADGRAPH5_AMC@NLO+MCFM. The shaded areas on all the panels represent the full uncertainties calculated as the quadratic sum of the statistical and systematic uncertainties, while the crosses represent the statistical uncertainties only.

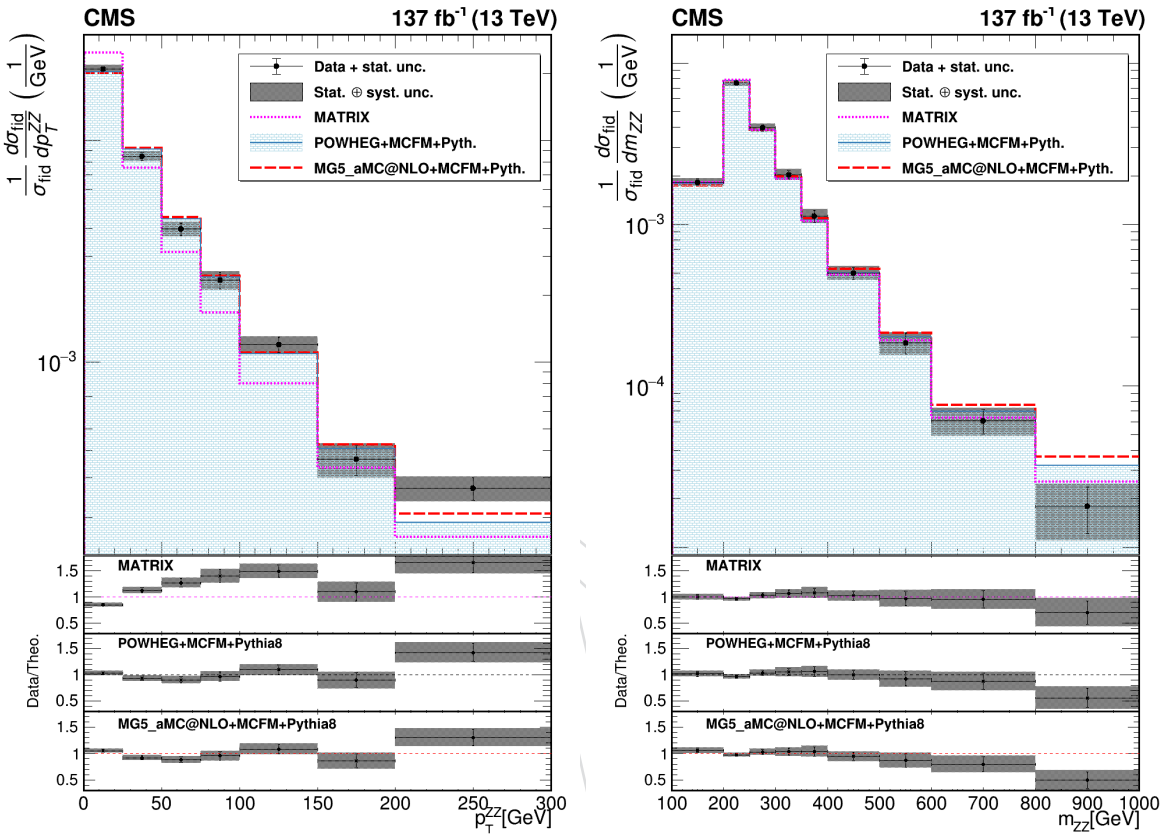

Figure 5: Differential cross sections normalized to the fiducial cross section for the combined 4e, 4μ, and 2e2μ decay channels as a function of (left) p_{T} of the ZZ system, (right) the invariant mass of the ZZ system. Points represent the unfolded data, the shaded histogram represent the POWHEG +MCFM ZZ predictions, and the dashed curves correspond to the results of the MATRIX and MADGRAPH5_AMC@NLO+MCFM calculations. The three lower panels represent the ratio of the measured cross section to the expected distributions from MATRIX, POWHEG +MCFM and MADGRAPH5_AMC@NLO+MCFM. The shaded areas on all the panels represent the full uncertainties calculated as the quadratic sum of the statistical and systematic uncertainties, while the crosses represent the statistical uncertainties only.

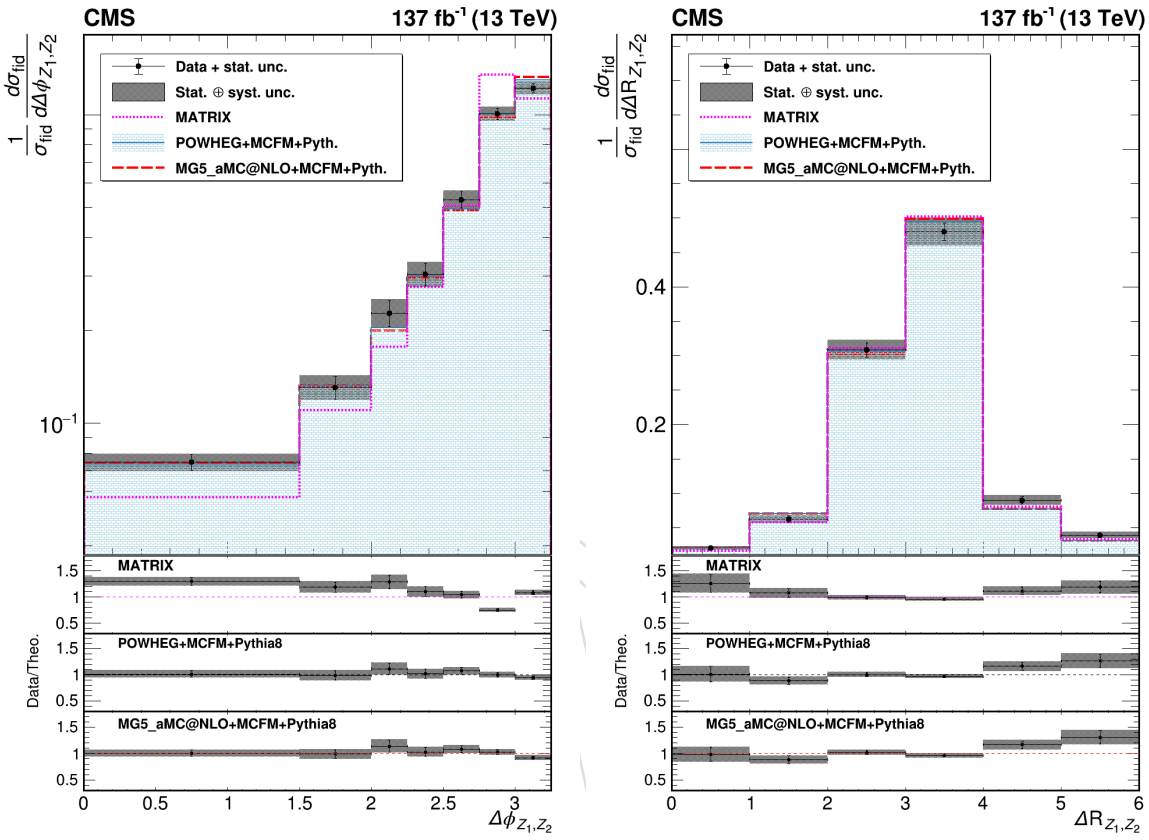

Figure 6: Differential cross sections normalized to the fiducial cross section for the combined 4e, 4μ, and 2e2μ decay channels as a function of azimuthal separation of the two Z bosons and ΔR between the Z-bosons. Points represent the unfolded data, and the shaded histogram represent the POWHEG +MCFM ZZ predictions, and the dashed curves correspond to the results of the MATRIX and MADGRAPH5_AMC@NLO+MCFM calculations. The three lower panels represent the ratio of the measured cross section to the expected distributions from MATRIX, POWHEG +MCFM and MADGRAPH5_AMC@NLO+MCFM. The shaded areas on all the panels represent the full uncertainties calculated as the quadratic sum of the statistical and systematic uncertainties, while the crosses represent the statistical uncertainties only.

(masses below 1000 GeV). Presence of aTGC increases the expected event yields at masses above 1300 GeV.

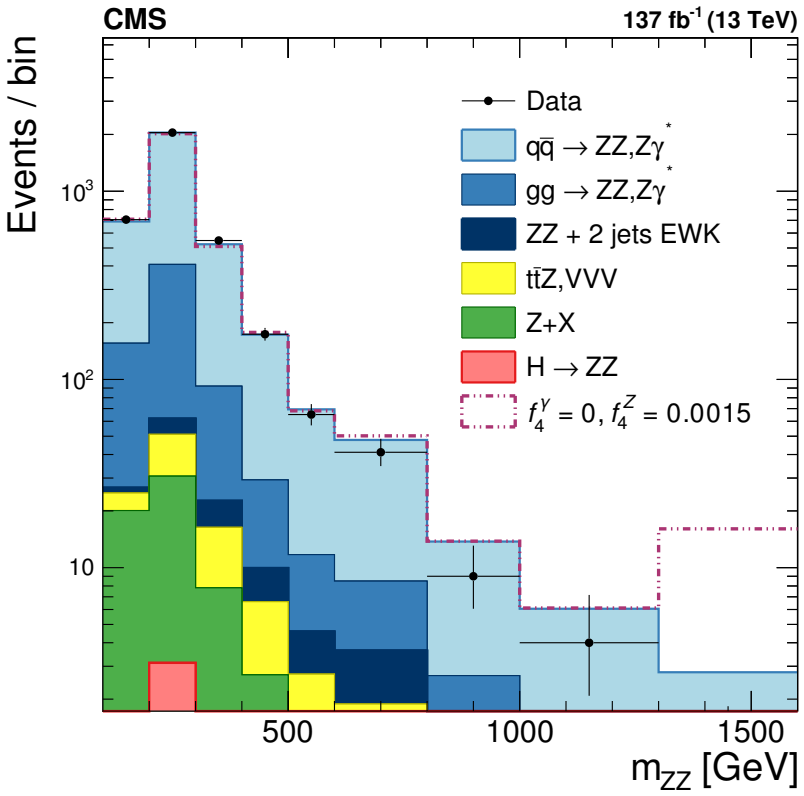

Figure 7: Distribution of the reconstructed ZZ mass for the combined 4e, 4μ, and 2e2μ channels. Points represent the data, the shaded histograms represent the SM prediction including signal and irreducible background from simulation, and the data-driven background estimate. Dashed histograms represent an example aTGC signal. The last bin includes contribution from all events with mass above 1.3 TeV.

The invariant mass distributions are interpolated from those obtained from the SHERPA simulation for different values of the anomalous couplings in the range between 0 and 0.03. For each distribution, only one or two couplings are varied while all others are set to zero, thus creating a grid of points in the (f_4^Z, f_4^γ) and (f_5^Z, f_5^γ) parameter planes and corresponding invariant mass distributions. In each $m_{4\ell}$ bin, expected signal values are interpolated between the 2D grid points using a second-order polynomial, since the cross section for the signal depends quadratically on the coupling parameters. A profile likelihood method [54] is used to derive the limits. Systematic uncertainties are taken into account by varying the number of expected signal and background events within their uncertainties. No form factor is used when deriving the limits so that the results do not depend on any assumed energy scale characterizing new physics. The constraints on anomalous couplings are displayed in Fig. 8. The curves indicate 68% and 95% CLs; the dots indicate where the likelihoods reach their maximum. Coupling values outside the contours are excluded at the corresponding CLs. The cross in the middle represent the observed 1D limits that are summarized in Table 5. The sensitivity is dominated by statistical uncertainties.

Complete one-loop electroweak (EW) corrections to massive vector boson pair production [56, 57] were applied as a cross check. The consequences of the EW corrections to ZZ production are that the ZZ mass spectrum falls more rapidly towards high masses. In addition, the

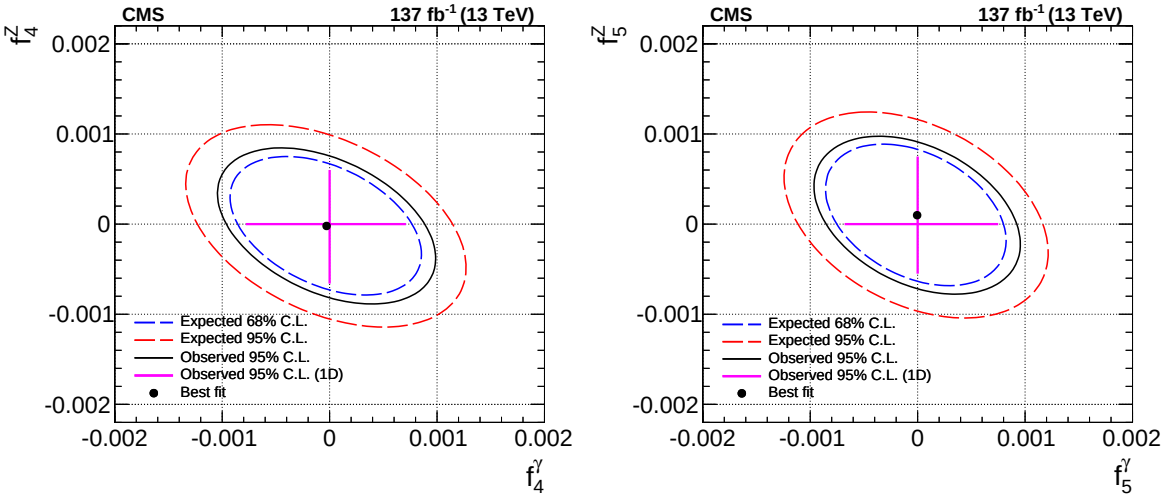

Figure 8: Two-dimensional observed (solid) and expected (dashed) contours exclusion limits at 95% CL, and at 68% and 95% CL, respectively, on the ZZZ and ZZγ aTGCs. The plots show the exclusion contours in the $(f^Z_{4(5)}, f^\gamma_{4(5)})$ parameter planes. Dots show where the likelihoods reach their maximum. The coupling values outside the contours are excluded at the corresponding confidence level. The crosses in the middle represent the observed 1D limits. No form factor is used.

Table 5: Expected and observed one-dimensional 95% CL limits on aTGC parameters. The corresponding constrains on EFT parameters are estimated using the transformation from Ref. [55].

	Expected 95% CL	Observed 95% CL
aTGC parameter	$\times 10^{-4}$	$\times 10^{-4}$
f_4^Z	-8.8 ; 8.3	-6.6 ; 6.0
f_5^Z	- 8.0 ; 9.9	-5.5 ; 7.5
f_4^γ	-10.0 ; 9.5	-7.8 ; 7.1
f_5^γ	-9.2 ; 9.8	-6.8 ; 7.5
EFT parameter	TeV^{-4}	TeV^{-4}
$C_{\tilde{B}W}/\Lambda^4$	-3.1 ; 3.3	-2.3 ; 2.5
C_{WW}/Λ^4	-1.7 ; 1.6	-1.4 ; 1.2
C_{BW}/Λ^4	-1.8 ; 1.9	-1.4 ; 1.3
C_{BB}/Λ^4	-1.6 ; 1.6	-1.2 ; 1.2

overall cross section decreases by about 4%. The effect of NLO EW corrections is estimated by reweighting the SM SHERPA sample as a function of $m_{4\ell}$ using weights derived from the calculations described in Ref. [56]. It is found to improve the expected limits by about 4–6%.

These results can be also expressed in terms of parameters calculated within effective field theory (EFT) framework, i.e. Ref. [58] and references therein. In contrast to anomalous couplings of electroweak vector bosons, the EFT framework allows for the unambiguous calculation of loop effects and is argued to be cleaner and simpler than that of anomalous couplings. The numerical relations between aTCGs and EFT parameters are given in Ref. [55]. The expected and measured limits in terms of EFT are presented in Table 5.

11 Summary

Results have been presented for a study of four-lepton final states in proton-proton collisions at $\sqrt{s} = 13\,\text{TeV}$ with the CMS detector at the LHC. The measured $\mathrm{pp} \to \mathrm{ZZ}$ cross section is $\sigma_{tot}(pp \to ZZ) = 17.2 \pm 0.3\,(\text{stat}) \pm 0.5\,(\text{syst}) \pm 0.4\,(\text{theo}) \pm 0.3\,(\text{lumi})$ pb, where the Z boson masses are in the range $60 < m_Z < 120\,\text{GeV}$. The results agree with SM predictions. The differential cross sections also agree well with the SM predictions. Improved limits on anomalous ZZZ and ZZγ triple gauge couplings are established, significantly restricting their allowed ranges.

References

[1] K. Hagiwara, R. D. Peccei, and D. Zeppenfeld, "Probing the weak boson sector in $e^+e^- \to W^+W^-$", *Nucl. Phys. B* **282** (1987) 253, doi:10.1016/0550-3213(87)90685-7.

[2] G. J. Gounaris, J. Layssac, and F. M. Renard, "New and standard physics contributions to anomalous Z and γ self-couplings", *Phys. Rev. D* **62** (2000) 073013, doi:10.1103/PhysRevD.62.073013, arXiv:hep-ph/0003143.

[3] CMS Collaboration, "Measurement of the ZZ production cross section and search for anomalous couplings in $2\ell 2\ell'$ final states in pp collisions at $\sqrt{s} = 7\,\text{TeV}$", *JHEP* **01** (2013) 063, doi:10.1007/JHEP01(2013)063, arXiv:1211.4890.

[4] CMS Collaboration, "Measurement of the $\mathrm{pp} \to \mathrm{ZZ}$ production cross section and constraints on anomalous triple gauge couplings in four-lepton final states at $\sqrt{s} = 8\,\text{TeV}$", *Phys. Lett. B* **740** (2015) 250, doi:10.1016/j.physletb.2014.11.059, arXiv:1406.0113. [Corrigenum: doi:10.1016/j.physletb.2016.04.010].

[5] CMS Collaboration, "Measurements of the ZZ production cross sections in the $2\ell 2\nu$ channel in proton-proton collisions at $\sqrt{s} = 7$ and 8 TeV and combined constraints on triple gauge couplings", *Eur. Phys. J. C* **75** (2015) 511, doi:10.1140/epjc/s10052-015-3706-0, arXiv:1503.05467.

[6] CMS Collaboration, "Measurement of the ZZ production cross section and $\mathrm{Z} \to \ell^+\ell^-\ell'^+\ell'^-$ branching fraction in pp collisions at $\sqrt{s} = 13\,\text{TeV}$", *Phys. Lett. B* **763** (2016) 280, doi:10.1016/j.physletb.2016.10.054, arXiv:1607.08834.

[7] CMS Collaboration, "Measurements of the $\mathrm{pp} \to \mathrm{ZZ}$ production cross section and the $\mathrm{Z} \to 4\ell$ branching fraction, and constraints on anomalous triple gauge couplings at

$\sqrt{s} = 13\,\text{TeV}$", *Eur. Phys. J. C* **78** (2018) 165, doi:10.1140/epjc/s10052-018-5567-9, 10.1140/epjc/s10052-018-5769-1, arXiv:1709.08601. [Erratum: Eur. Phys. J.C78,no.6,515(2018)].

[8] ATLAS Collaboration, "Measurement of ZZ production in pp collisions at $\sqrt{s} = 7\,\text{TeV}$ and limits on anomalous ZZZ and ZZγ couplings with the ATLAS detector", *JHEP* **03** (2013) 128, doi:10.1007/JHEP03(2013)128, arXiv:1211.6096.

[9] ATLAS Collaboration, "Measurements of four-lepton production in pp collisions at $\sqrt{s} = 8\,\text{TeV}$ with the ATLAS detector", *Phys. Lett. B* **753** (2016) 552, doi:10.1016/j.physletb.2015.12.048, arXiv:1509.07844.

[10] ATLAS Collaboration, "Measurement of the ZZ production cross section in pp collisions at $\sqrt{s} = 13\,\text{TeV}$ with the ATLAS detector", *Phys. Rev. Lett.* **116** (2016) 101801, doi:10.1103/PhysRevLett.116.101801, arXiv:1512.05314.

[11] ATLAS Collaboration, "Measurement of the four-lepton invariant mass spectrum in 13 TeV proton-proton collisions with the ATLAS detector", *JHEP* **04** (2019) 048, doi:10.1007/JHEP04(2019)048, arXiv:1902.05892.

[12] ATLAS Collaboration, "Measurement of ZZ production in the $\ell\ell\nu\nu$ final state with the ATLAS detector in pp collisions at $\sqrt{s} = 13\,\text{TeV}$", *JHEP* **10** (2019) 127, doi:10.1007/JHEP10(2019)127, arXiv:1905.07163.

[13] ATLAS Collaboration, "$ZZ \to \ell^+\ell^-\ell'^+\ell'^-$ cross-section measurements and search for anomalous triple gauge couplings in 13 TeV pp collisions with the ATLAS detector", *Phys. Rev. D* **97** (2018) 032005, doi:10.1103/PhysRevD.97.032005, arXiv:1709.07703.

[14] F. Cascioli et al., "ZZ production at hadron colliders in NNLO QCD", *Phys. Lett. B* **735** (2014) 311, doi:10.1016/j.physletb.2014.06.056, arXiv:1405.2219.

[15] CMS Collaboration, "The CMS experiment at the CERN LHC", *JINST* **3** (2008) S08004, doi:10.1088/1748-0221/3/08/S08004.

[16] CMS Collaboration, "Performance of electron reconstruction and selection with the CMS detector in proton-proton collisions at $\sqrt{s} = 8\,\text{TeV}$", *JINST* **10** (2015) P06005, doi:10.1088/1748-0221/10/06/P06005, arXiv:1502.02701.

[17] CMS Collaboration, "Performance of CMS muon reconstruction in pp collision events at $\sqrt{s} = 7\,\text{TeV}$", *JINST* **7** (2012) P10002, doi:10.1088/1748-0221/7/10/P10002, arXiv:1206.4071.

[18] CMS Collaboration, "Performance of the CMS muon detector and muon reconstruction with proton-proton collisions at $\sqrt{s} = 13\,\text{TeV}$", *JINST* **13** (2018) P06015, doi:10.1088/1748-0221/13/06/P06015, arXiv:1804.04528.

[19] S. Alioli, P. Nason, C. Oleari, and E. Re, "NLO vector-boson production matched with shower in POWHEG", *JHEP* **07** (2008) 060, doi:10.1088/1126-6708/2008/07/060, arXiv:0805.4802.

[20] P. Nason, "A new method for combining NLO QCD with shower Monte Carlo algorithms", *JHEP* **11** (2004) 040, doi:10.1088/1126-6708/2004/11/040, arXiv:hep-ph/0409146.

[21] S. Frixione, P. Nason, and C. Oleari, "Matching NLO QCD computations with parton shower simulations: the POWHEG method", *JHEP* **11** (2007) 070, doi:10.1088/1126-6708/2007/11/070, arXiv:0709.2092.

[22] S. Alioli, P. Nason, C. Oleari, and E. Re, "A general framework for implementing NLO calculations in shower Monte Carlo programs: the POWHEG BOX", *JHEP* **06** (2010) 043, doi:10.1007/JHEP06(2010)043, arXiv:1002.2581.

[23] T. Melia, P. Nason, R. Rontsch, and G. Zanderighi, "W^+W^-, WZ and ZZ production in the POWHEG BOX", *JHEP* **11** (2011) 078, doi:10.1007/JHEP11(2011)078, arXiv:1107.5051.

[24] J. M. Campbell and R. K. Ellis, "MCFM for the Tevatron and the LHC", *Nucl. Phys. B Proc. Suppl.* **10** (2010) 205, doi:10.1016/j.nuclphysbps.2010.08.011, arXiv:1007.3492.

[25] F. Caola, K. Melnikov, R. Röntsch, and L. Tancredi, "QCD corrections to ZZ production in gluon fusion at the LHC", *Phys. Rev. D* **92** (2015) 094028, doi:10.1103/PhysRevD.92.094028, arXiv:1509.06734.

[26] Y. Gao et al., "Spin determination of single-produced resonances at hadron colliders", *Phys. Rev. D* **81** (2010) 075022, doi:10.1103/PhysRevD.81.075022, arXiv:1001.3396.

[27] S. Bolognesi et al., "Spin and parity of a single-produced resonance at the LHC", *Phys. Rev. D* **86** (2012) 095031, doi:10.1103/PhysRevD.86.095031, arXiv:1208.4018.

[28] I. Anderson et al., "Constraining anomalous HVV interactions at proton and lepton colliders", *Phys. Rev. D* **89** (2014) 035007, doi:10.1103/PhysRevD.89.035007, arXiv:1309.4819.

[29] J. Alwall et al., "The automated computation of tree-level and next-to-leading order differential cross sections, and their matching to parton shower simulations", *JHEP* **07** (2014) 079, doi:10.1007/JHEP07(2014)079, arXiv:1405.0301.

[30] R. Frederix and S. Frixione, "Merging meets matching in MC@NLO", *JHEP* **12** (2012) 061, doi:10.1007/JHEP12(2012)061, arXiv:1209.6215.

[31] T. Gleisberg et al., "Event generation with SHERPA 1.1", *JHEP* **02** (2009) 007, doi:10.1088/1126-6708/2009/02/007, arXiv:0811.4622.

[32] T. Sjöstrand et al., "An introduction to PYTHIA 8.2", *Comput. Phys. Commun.* **191** (2015) 159, doi:10.1016/j.cpc.2015.01.024, arXiv:1410.3012.

[33] CMS Collaboration, "Extraction and validation of a new set of CMS PYTHIA8 tunes from underlying-event measurements", Technical Report CMS-PAS-GEN-17-001, CERN, Geneva, 2018.

[34] CMS Collaboration, "Event generator tunes obtained from underlying event and multiparton scattering measurements", *Eur. Phys. J. C* **76** (2016) 155, doi:10.1140/epjc/s10052-016-3988-x, arXiv:1512.00815.

[35] NNPDF Collaboration, "Parton distributions from high-precision collider data", *Eur. Phys. J. C.* **77** (2017) 663, doi:10.1140/epjc/s10052-017-5199-5, arXiv:1706.00428.

[36] GEANT4 Collaboration, "GEANT4—a simulation toolkit", *Nucl. Instrum. Meth. A* **506** (2003) 250, doi:10.1016/S0168-9002(03)01368-8.

[37] CMS Collaboration, "Particle-flow reconstruction and global event description with the CMS detector", *JINST* **12** (2017) P10003, doi:10.1088/1748-0221/12/10/P10003, arXiv:1706.04965.

[38] M. Cacciari, G. P. Salam, and G. Soyez, "The Anti-k_t jet clustering algorithm", *JHEP* **04** (2008) 063, doi:10.1088/1126-6708/2008/04/063, arXiv:0802.1189.

[39] M. Cacciari, G. P. Salam, and G. Soyez, "FastJet user manual", *Eur. Phys. J. C* **72** (2012) 1896, doi:10.1140/epjc/s10052-012-1896-2, arXiv:1111.6097.

[40] CMS Collaboration, "Technical proposal for the phase-II upgrade of the Compact Muon Solenoid", CMS Technical proposal CERN-LHCC-2015-010, CMS-TDR-15-02, CERN, 2015.

[41] M. Cacciari and G. P. Salam, "Pileup subtraction using jet areas", *Phys. Lett. B* **659** (2008) 119, doi:10.1016/j.physletb.2007.09.077, arXiv:0707.1378.

[42] CMS Collaboration, "Measurement of the inclusive W and Z production cross sections in pp collisions at $\sqrt{s} = 7$ TeV", *JHEP* **10** (2011) 132, doi:10.1007/JHEP10(2011)132, arXiv:1107.4789.

[43] CMS Collaboration, "The CMS trigger system", *JINST* **12** (2017) P01020, doi:10.1088/1748-0221/12/01/P01020, arXiv:1609.02366.

[44] CMS Collaboration, "Measurement of the properties of a Higgs boson in the four-lepton final state", *Phys. Rev. D* **89** (2014) 092007, doi:10.1103/PhysRevD.89.092007, arXiv:1312.5353.

[45] Particle Data Group, C. Patrignani et al., "Review of particle physics", *Chin. Phys C* **40** (2016) 100001, doi:10.1088/1674-1137/40/10/100001.

[46] J. Butterworth et al., "PDF4LHC recommendations for LHC Run II", *J. Phys. G* **43** (2016) 023001, doi:10.1088/0954-3899/43/2/023001, arXiv:1510.03865.

[47] NNPDF Collaboration, "Parton distributions for the LHC run II", *JHEP* **04** (2015) 040, doi:10.1007/JHEP04(2015)040, arXiv:1410.8849.

[48] CMS Collaboration, "CMS luminosity measurement for the 2017 data-taking period", CMS Physics Analysis Summary CMS-PAS-LUM-17-001, CERN, 2017.

[49] CMS Collaboration, "CMS luminosity measurement for the 2017 data-taking period at $\sqrt{s}$ = 13 tev", CMS Physics Analysis Summary CMS-PAS-LUM-17-004, CERN, 2017.

[50] CMS Collaboration, "CMS luminosity measurement for the 2017 data-taking period at $\sqrt{s}$ = 13 tev", CMS Physics Analysis Summary CMS-PAS-LUM-18-002, CERN, 2018.

[51] M. Grazzini, S. Kallweit, and D. Rathlev, "ZZ production at the LHC: fiducial cross sections and distributions in NNLO QCD", *Phys. Lett. B* **750** (2015) 407, doi:10.1016/j.physletb.2015.09.055, arXiv:1507.06257.

[52] M. Grazzini, S. Kallweit, and M. Wiesemann, "Fully differential NNLO computations with MATRIX", *Eur. Phys. J. C* **78** (2018) 537, doi:10.1140/epjc/s10052-018-5771-7, arXiv:1711.06631.

[53] T. Adye, "Unfolding algorithms and tests using RooUnfold", in *Proceedings, PHYSTAT 2011 Workshop on Statistical Issues Related to Discovery Claims in Search Experiments and Unfolding*, H. Prosper and L. Lyons, eds., p. 313, CERN. Geneva, Switzerland, 17–20 January, 2011. arXiv:1105.1160. doi:10.5170/CERN-2011-006.313.

[54] Particle Data Group Collaboration, "Review of particle physics (rpp)", *Phys. Rev. D* **86** (2012) 010001, doi:10.1103/PhysRevD.86.010001.

[55] C. Degrande, "A basis of dimension-eight operators for anomalous neutral triple gauge boson interactions", *JHEP* **02** (2014) 101, doi:10.1007/JHEP02(2014)101, arXiv:1308.6323.

[56] A. Bierweiler, T. Kasprzik, and J. H. Kuhn, "Vector-boson pair production at the LHC to $\mathcal{O}(\alpha^3)$ accuracy", *JHEP* **12** (2013) 071, doi:10.1007/JHEP12(2013)071, arXiv:1305.5402.

[57] J. Baglio, L. D. Ninh, and M. M. Weber, "Massive gauge boson pair production at the LHC: a next-to-leading order story", *Phys. Rev. D* **88** (2013) 113005, doi:10.1103/PhysRevD.88.113005, arXiv:1307.4331.

[58] C. Degrande et al., "Effective Field Theory: A Modern Approach to Anomalous Couplings", *Annals Phys.* **335** (2013) 21, doi:10.1016/j.aop.2013.04.016, arXiv:1205.4231.